Energetic electron precipitation associated with pulsating aurora: EISCAT and Van Allen Probe observations

Y. Miyoshi (1), S. Oyama (1), S. Saito (2) S. Kurita (1), H. Fujiwara (3), R. Kataoka (4), Y. Ebihara (5), C. Kletzing (6), G. Reeves (7), O. Santolik (8,9), M. Clilverd (10), C. J. Rodger (11), E. Turunen (12), and F. Tsuchiya (13)

(1) Solar-Terrestrial Environment Laboratory, Nagoya University, Japan
(2) Graduate School of Science, Nagoya University, Japan
(3) Seikei University, Japan
(4) National Institute of Polar Research, Japan
(5) Research Institute for Sustainable Humanosphere, Kyoto University, Japan
(6) University of Iowa, Iowa, USA.
(7) Los Alamos National Laboratory, Los Alamos, NM, USA
(8) Institute of Space Science, Insitute of Atmospheric Physics, Czech Rep.
(9) Faculty of Mathematics and Physics, Charles University in Prague, Czech Rep.
(10) British Antarctic Survey, Cambridge,UK
(11) Department of Physics, University of Otago, Dunedin, New Zealand
(12) Sodankyla Geophysical Observatory, University of Oulu, Finland
(13) Planetary Plasma and Atmospheric Research Center, Tohoku University, Japan

Abstract:

Pulsating auroras show quasi-periodic intensity modulations caused by the precipitation of energetic electrons of the order of tens of keV. It is expected theoretically that not only these electrons but also sub-relativistic/relativistic electrons precipitate simultaneously into the ionosphere owing to whistler-mode wave–particle interactions. The height-resolved electron density profile was observed with the European Incoherent Scatter (EISCAT) Tromsø VHF radar on **17 November 2012**. Electron density enhancements were clearly identified at altitudes >68 km in association with the pulsating aurora, suggesting precipitation of electrons with a broadband energy range from ~10 keV up to at least 200 keV. **The riometer and network of subionospheric radio wave observations also showed the energetic electron precipitations during this period.** During this period, the footprint of the Van Allen Probe-A satellite was very close to Tromsø and the satellite observed rising tone emissions of the lower-band chorus (LBC) waves near the equatorial plane. Considering the observed LBC waves and electrons, we conducted a computer simulation of the wave–particle interactions. This showed **simultaneous precipitation of** electrons at both tens of keV and a few hundred keV, which is consistent with the energy spectrum estimated by the inversion method using the EISCAT observations. This result revealed that electrons **with a wide energy range** simultaneously precipitate into the ionosphere in association with the pulsating aurora, **providing the evidence that pulsating auroras are caused by whistler chorus waves. We suggest that scattering by propagating whistler simultaneously causes both the precipitations of sub-relativistic electrons and the pulsating aurora.**

1. Introduction

Pulsating auroras show quasi-periodic intensity modulations of extended forms that are caused by the precipitation of energetic electrons [e.g., Lessard, 2012, Li et al., 2012]. Sounding rockets as well as the FAST and Reimei satellites have confirmed that pulsating auroras are caused by quasi-periodical precipitation of electrons with energies from a few keV to tens of keV [e.g., Sandahl et al., 1980, Sato et al., 2004, Miyoshi et al., 2010, Nishiyama et al., 2011]. **Reinard et al.** [1997] used sounding rocket observations to show that electrons at ~150 keV precipitate into the ionosphere in association with pulsating auroras. **The whistler-mode chorus waves [e.g., Nishimura et al., 2010] and electron cyclotron harmonic (ECH) waves [e.g., Liang et al., 2010] are thought to be important mechanisms to cause the precipitation of electrons associated with the pulsating aurora.**

Recently, Miyoshi et al. [2010] proposed a time-of-flight (TOF) model that considers whistler mode chorus waves propagating along the field lines. Because the wave–particle resonant energy depends on magnetic latitude, electrons are potentially scattered with **a wide energy range** along the field lines. **Figure 1** illustrates the concept of the model. Whistler mode chorus waves that are generated at the equator firstly drive the pitch angle scattering of ~10 keV electron, which causes the pulsating aurora (Figure 1(a)). Subsequently, the waves propagate to higher latitudes and pitch angle scattering with sub-relativistic (~few hundreds of keV) /relativistic electrons (~MeV) take place (Figure 1(b)).

This model has been used to estimate the source region of pulsating electrons observed by the Reimei satellite [Miyoshi et al., 2010, Nishiyama et al., 2011], and the model has been extended to the relativistic energy range [Saito et al., 2012]. The model indicates that whistler-mode waves first resonate with electrons at tens of keV near the equator, and then with higher-energy electrons at higher latitudes [Horne and Thorne, 2003]; therefore, precipitation of electrons across **a wide energy range** is expected.

The precipitation of energetic electrons by chorus waves has been studied using computer simulations. Hikishima et al. [2010] performed a self-consistent particle-in-cell simulation for the chorus wave–particle interactions, and they indicated that microbursts of 10–100 keV electrons are caused by chorus rising tones. Saito et al. [2012] developed the test particle simulation code GEMSIS-RBW, and they showed simulated resonant interactions between energetic electrons and whistler-mode chorus waves, including nonlinear wave–particle interactions. They reproduced MeV electron microbursts due to chorus wave–particle interactions, and they found modulations of a few Hz embedded in the precipitating electron flux variations, which are associated with the repetition period of the chorus elements. This result is consistent with the model of Miyoshi et al. [2010].

ECH waves, which represent another candidate mechanism for pulsating auroras, do not resonate with sub-relativistic and relativistic electrons [e.g., Thorne et al., 2010]. If ECH waves are a dominant process in causing a pulsating aurora, then the absence of sub-relativistic electron precipitation associated with the pulsating aurora is to be expected. On the other hand, it would be expected that **a wide energy range** electrons would precipitate into the atmosphere associated with a pulsating aurora, if the chorus waves were the primary driver behind pitch-angle scattering.

Therefore, measurement of the maximum energy of the precipitating electrons associated with a pulsating aurora is essential to distinguish the primary mechanisms behind pulsating auroras. Although measurements of precipitating electrons with **a wide energy range** from a few keV to MeV have not been obtained by satellites, observations of the height-resolved electron density profile at night should be a good proxy for precipitating electrons with the highest energy. For example, the stopping heights of 100, 200, and ~400 keV electrons are ~75, ~68, and ~63 km, respectively, and the stopping height of monoenergetic beams of 1 MeV electrons is below 60 km [e.g., Turunen et al., 2009, **Cresswell-Moorcock et al., 2013, Simon Wedlund et al., 2014, Kero et al., 2014**].

As with previous observations for the height-resolved electron density profile associated with pulsating auroras, Jones et al. [2009], using the Poker Flat Incoherent Scatter Radar, showed that significant electron density enhancement appears at an altitude of 90 km which indicates precipitation of ~20 keV electrons [Semeter and Kamalabadi, 2005].

Oyama et al. [2014] reported on the characteristics of the electron density profile of the E-layer and F-layer and found a C-form structure to the density profile, indicating that soft-electron (<1 keV) precipitation occurs simultaneously in association with hard-electron (~keV) precipitation in the pulsating aurora.

In this study, we observe the height-resolved electron density variations using the European Incoherent Scatter (EISCAT) radar **at Tromsø** to identify the precipitating energy of electrons associated with pulsating auroras. We also use the data from the network of subionospheric radio receiver sites and riometers to observe energetic electron precipitations during the period. Moreover, we investigate the plasma waves and electrons in the magnetosphere during the event using Van Allen Probe-A satellite data [Mauk et al., 2012]. Using the plasma wave and energetic electron data from Van Allen Probe-A as inputs to the simulation, we conduct a test particle simulation of pitch-angle scattering by whistler-mode chorus waves and assess the consideration that the observed whistler-mode chorus waves cause both the pulsating auroras (precipitation of tens keV electrons) as well as the sub-relativistic electron precipitation.

2. Ground-based Observations: EISCAT/Riometer/Sub-Ionospheric Radio Waves

At 04:00–06:00 UT on **17 November 2012**, a pulsating aurora was observed in Tromsø, Norway (69.35ºN, 19.14ºE). The magnetic local time was 06:30–08:30, i.e., the pulsating aurora occurred on the morning side. The invariant latitude of Tromsø is 66.12º. During the pulsating aurora event, the Kp index was 3. The AL index and geomagnetic field at the IMAGE Magnetometer Array in Tromsø showed that several enhancements of westward electrojets were found during the period (not shown), indicating substorm activity, and the pulsating aurora in this event occurred during the period from the late expansion phase to the recovery phase of the substorm. Note that a weak electron injection was detected at geosynchronous orbit at ~0400UT (not shown).

The EISCAT VHF radar transmitted an alternating-coded pulse with 61 bits of 2.4 microsecond baud length or 146.4 microsecond pulse length, corresponding to 21.96 km in range. The received signal was dumped every 4.8 seconds, and incoherent scatter spectra were integrated for 60 seconds to obtain the ionospheric

parameters with Grand Unified Incoherent Scatter Design and Analysis Package (GUISDAP) [Lehtinen and Huuskonen, 1996]. The electron density can also be estimated from the backscatter echo power in the D region and below, and it was applied to make Figures 2a and 3.

Figure 2(a) shows the time variations in the height profile of the electron density from vertical measurements of the EISCAT VHF radar. Enhanced electron density was observed after 04:30 UT, and the density enhancement region expanded to an altitude of 68 km. The optical digital camera and photometer installed at Tromsø were used to identify the pulsating aurora during the period. **Figure 2(b)** shows examples of all-sky images; pulsating auroras were widely observed over Tromsø during the period of enhanced electron density in the D region. The five orange lines result from the backscatter of lidar beams. **Figure 2(c)** shows the time variation in the optical intensity at 427.8 nm from the photometer, which was oriented to the local magnetic zenith, whose angle is 12 deg from the local zenith. The sampling rate of the photometer was 50 ms, and seven-point running average was used to smooth the variation. Quasi-periodical ON–OFF variations are found at 427.8 nm. From the frequency spectrum analysis, periods of 5~10 s are identified as the main optical modulations that embed the 3-Hz internal modulations.

The yellow and red rectangles in **Figure 2(b)** indicate the direction of the field-of-view of the EISCAT VHF radar and the photometer, respectively. Both instruments observed almost **the same direction**; therefore, the density enhancements measured by EISCAT were actually caused by electron precipitation in the pulsating aurora.

To investigate the altitude profile of the electron density in detail, **Figure 3** shows the averaged electron density profiles during the period both without the pulsating aurora (03:00–03:22 UT) and with the pulsating aurora (04:30–04:52 UT). **Figure 3(a)** shows large density enhancements in the E-layer at ~100 km during the period with the pulsating aurora, most likely resulting from ionization by the energetic electron precipitation. **Figure 3(b)** is the same as **Figure 3(a)** but shows the profile from 60 to 80 km. During the period without the pulsating aurora, the electron density is $\sim 3\times 10^{8}$, $\sim 10^{9}$, and $\sim 10^{10}$ m^{-3} at 70, 80, and 100 km, respectively. During the period with the pulsating aurora, the electron density increases greatly owing to ionization by the energetic electron precipitation. The electron density in the lower ionosphere is $\sim 6\times10^{8}$, $\sim 3\times10^{10}$, and $\sim 2.5\times10^{11}$ m^{-3} at 70, 80, and 100 km, respectively, and the highest density was observed at ~100 km. A comparison of the electron density profiles for the periods both with and without the pulsating aurora reveals that the EISCAT VHF radar detected clearly electron density enhancement at >68 km.

Figure 4 shows the network of subionospheric radio wave receiver sites operated by the Antarctic-Arctic Radiation-belt (Dynamic) Deposition -VLF Atmospheric Research Konsortium, AARDDVARK (Clilverd et al., 2009), as well as the great circle paths between transmitters and the receiver stations. From the AARDDVARK observations, >50 keV electron precipitation was detected during 04-05 UT along the great circle paths between NAA (Maine, USA, 44.58 °N, 293.2°E) and Sodankyla, NRK (Reykjavik, Iceland, 63.85 °N, 338.4 °E) and Sodankyla, as well as NAA to Ny Alesund (Svalbard, 78.93 °N, 11.95 °E). The great circle paths of some of these subionospheric radio waves pass through the precipitation region observed by EISCAT, and suggest that the event included significant precipitation flux of >50 keV. The shaded area in Figure 4 corresponds to the inferred region of the precipitation, using observations from many AARDDVARK paths. From the AARDDVARK network observations, it is concluded that precipitation occurred over at least ~75 degrees of the longitude, i.e., from 01 MLT at Newfoundland to 07 MLT at Sodankyla. Similar network observation (operated by Tohoku University, Japan) confirmed this result by the observations between NRK and Ny Alesund, Jainfingen (Germany, 50.01 °N, 9.01 °E) and Ny Alesund, and Anthorn (UK, 54.92 °N, 356.75 °E) and Ny Alesund. Since there are no paths east of Sodankyla, it is not possible to discuss the eastern longitude limit of the precipitation.

It is worthwhile to note that the 30 MHz, wide beam riometers at Abisko, Sweden (68.35°N, 18.83°E), Ivalo, Finland (68.65 °N, 27.54 °E) detected absorption between 1.0-1.3 dB during the event (not shown). Calculation of riometer absorption using the perturbed and non-perturbed EISCAT electron density profiles following the technique described in Rodger et al. [2012] gives 1.3 dB, which is consistent with

the absorption levels observed.

3. Observations from Van Allen Probe-A

During the period, the Van Allen Probe-A satellite traversed the dawnside and **Figure 5** shows its footprint around Tromsø. The circle indicates the field-of-view of the all-sky camera at Tromsø, and the pulsating auroras were observed within this field-of-view.

Figure 6 shows a combined plot of the frequency spectrum from EMFISIS [Kletzing et al., 2013] and the electron energy spectrum from ECT/HOPE and MAGIES [Spence et al., 2013, Funsten et al.,2013, Blake et al., 2013]. **Figure 6(a)** shows the wave spectrum, from which the continuous banded emission of the upper-hybrid resonance (UHR) waves can be seen. The white line in the figure indicates the local electron-gyro frequency. The sudden increase of the UHR frequency around 06:30 UT indicates the crossing of the plasmapause, and the Van Allen Probe-A satellite was outside the plasmapause during the pulsating aurora event. The ratio of the plasma frequency to the electron-gyro frequency was 4~5 during the period. The emission around 1 kHz in **Figure 6(b)** is the whistler-mode waves below the local electron-gyro frequency. **Figure 6 (c) and (d) show the electron data from ECT/MagIES that measures electrons from 37 keV to 3869 keV for pitch angles of 90 deg and 24.5 deg respectively. Figure 6 (e) and (f) show the electron data from ECT/HOPE that measures electrons from 20 eV to 51 keV for pitch angles of 90 deg and 18.0 deg, respectively.** During the pulsating aurora period, **wide energy range electrons** up to MeV exist in the magnetosphere.

Figure 7 shows the wave-burst mode data of EMFISIS at 04:50 UT. The satellite observed the waveform with 6 s cadence. Clear rising tone emissions of the lower-band chorus (LBC) waves were observed during the time. The EMFISIS observations confirmed that the wave normal angles of these rising tones are almost parallel to the ambient magnetic field. **Analysis of EMFISIS observations by a technique [Santolik et al., 2003] showed that the wave vectors of the intense rising tones are almost anti-parallel to the ambient magnetic field. The Poynting flux analysis [Santolik et al., 2001] confirmed that the observed LBC waves propagate to the southern**

hemisphere.

4. Computer Simulations and Discussion

The EISCAT observations indicated enhanced electron density above an altitude of 68 km. According to the height profile of the stopping heights, the electron density enhancement at this altitude is caused by precipitation of electrons with energy of at least ~200 keV [Turunen et al., 2009], i.e., sub-relativistic electrons (~200 keV electrons) associated with the pulsating aurora precipitation into the ionosphere. **The observations from the network of subionospheric radio wave receiver showed >50 keV electron precipitations from 01 MLT to 07 MLT, and the riometer observations confirmed the energetic electron precipitations during the period.** Together with the observations at the ionospheric altitude, the observations from the Van Allen Probe-A satellite confirmed the rising tone chorus emissions outside the plasmapause near the equatorial plane.

Here, we investigate a possible mechanism for the simultaneous scattering of both electrons at tens of keV for the pulsating aurora and sub-relativistic electrons. Thorne et al. [2010] derived the pitch-angle diffusion coefficients for LBC, upper-band chorus (UBC), and ECH waves, and their work revealed that ECH waves mainly cause pitch-angle scattering of low-energy electrons and that they are ineffective for higher-energy electrons more than a few keV.

To evaluate whether chorus waves observed by Van Allen Probe-A can cause precipitation of electrons with **a wide energy range**, as observed by EISCAT, we conducted a GEMSIS-RBW simulation [Saito et al., 2012]. In this simulation, we used the observation data from the Van Allen Probe-A satellite as inputs.

The GEMSIS-RBW simulation was developed to solve electron motion and scattering along a magnetic field line. The magnetic mirror motion of an electron is described as the guiding center motion, while the electron momentum changes, associated with wave–particle interaction, are given by the following equation of motion:

$$\frac{d}{dt}\mathbf{p}_e = q\left(\delta\mathbf{E} - \mathbf{v}_e \times \left(\mathbf{B} + \delta\mathbf{B}\right)\right)$$

where $\mathbf{v}_e = \mathbf{p}_e / m_e\gamma$ is the electron velocity, γ is the relativistic Lorentz gamma, $\mathbf{B}$ is the background magnetic field vector at the electron guiding center position, $\mathbf{p}_e$ is the electron momentum, m_e is the electron rest mass, and $\delta\mathbf{E}$ and $\delta\mathbf{B}$ are the electric/magnetic fields of the chorus waves that satisfy the dispersion relation of the whistler-mode waves, which propagate along the field line. When the electron interacts with the chorus waves, the equation of motion is numerically solved with the time step δt during Δt, where δt is chosen to resolve the gyro-motion and Δt is the time step to solve the adiabatic guiding center motion. After calculating the momentum change Δp during Δt, the first adiabatic invariant of the electron at $t+\Delta t$ is calculated using the background magnetic field intensity at the electron's position. Simultaneously with the scattering process, the electron guiding center position is advanced in keeping with the first and second adiabatic invariants.

In this simulation, we modeled the rising tones of the LBC waves, as shown in **Figure 8(a)**. Considering the observations, we assumed the wave amplitude of 500 pT. It is difficult to determine the repetition period of the bursts from the observations of the Van Allen Probe-A satellite because the burst mode observations were intermittent. Thus, in this study, we assumed that the duration of each LBC burst was 2 s and that the repetition time was 7 s. Furthermore, it is assumed that LBC propagates to the magnetic latitude of 20 deg, based on the statistical analsyis [Meredith et al., 2012]. The magnetic field line for this simulation was the same L-shell as observed by the Van Allen Probe-A satellite (L = 5.7). The observed ratio of the plasma frequency to the electron-gyro frequency was used in the simulation, and the constant density distribution along the field line is assumed.

The test particles (512,000 electrons) were released along the dipole magnetic field line. They were distributed for all pitch angles along the field line with random bounce phase. Note that no electrons existed within the theoretical loss-cone angle defined at the altitude of the ionospheric absorption layer (100 km). In order to estimate the precipitated flux from our test-particle simulations, a weighting factor was considered for each test-particle as an initial condition.

We calculated the differential flux from the test-particles with the weighting factor, to be identical to the differential flux as measured by HOPE/MagIES of the Van Allen Probe-A satellite (see Figure 6). During the period, the Van Allen Probe-A satellite was at the magnetic latitude of -10 deg. Considering the conservation of the first adiabatic invariant, we convert the observed pitch angle to the equatorial pitch angle, and then we estimate the pitch angle distribution by assuming the functional form of $j\left(\alpha_{eq}\right) = j_0 \sin^n \alpha_{eq}$, where $j\left(\alpha_{eq}\right)$ is the differential flux at the equatorial pitch angle α_{eq}, j_0 is the differential flux at 90° pitch angle. Using the pitch angle distribution data of HOPE/MAGIES, we estimate j_0 and n for each energy, and then we use $j\left(\alpha_{eq}\right)$ as the initial distribution for the GEMSIS-RBW simulation. **Note that the loss cone angle at the position of the Van Allen Probe-A satellite is 3.5 deg, while the loss cone angle at the magnetic equator along the same field line is 3.0 deg.**

Using the EISCAT measured electron density profile, we estimate the energy spectra of precipitating electrons by the CARD inversion method [Brekke et al., 1989, Fujii et al., 1995]. **The method solves the continuity equation for the electron density n_e without the transportation and uses the MSIS-model as a neutral density profile. The model assumes the equilibrium between production and loss processes, that is, the loss rate can be written as $\alpha_{eff} \Delta n_e^2$, where α_{eff} is the effective recombination rate and the model calculates the electron density variations Δn_e by auroral particle precipitation. At polar winter night, Δn_e in the lower E region is almost equal to the EISCAT-measured electron density because of no other major ionization source except for the precipitation. Figure 8** (b) shows the energy spectrum of electrons observed near the magnetic equator from the Van Allen Probe-A satellite (blue triangle) and at the ionospheric altitude estimated from the CARD (red **triangle**). The CARD data show the energy spectrum during the period with the pulsating aurora (04:30–04:52 UT). **The statistical error of the estimated flux is about 2.5% below 100 keV and 20% above 100 keV during the period.** The corresponding pitch angle at energies from 10 keV to 51 keV (HOPE instrument) is 18 deg, while the pitch angle at energy above 56 keV is 24.5 deg (MagIES instrument) at the magnetic latitude of 10 deg. Comparing the energy spectrum between the magnetosphere and the ionosphere for the period with the pulsating aurora, the electron fluxes from a few keV up to 100 keV are almost same between them. This means that the pitch angle scattering occurred in the strong diffusion [Kennel, 1969] in which the flux between inside/outside the loss cone should be **almost the same**. On the other hand, the flux estimated from the CARD method is significantly smaller than that from the Van Allen Probe-A satellite observations above 100 keV, meaning that the pitch angle scattering rate becomes small at sub-relativistic energy range.

The precipitating flux at several energies calculated from the test-particle simulations is also shown in **Figure 8 (b).** The energy spectrum shows good agreement with the EISCAT observations. **Just like** the EISCAT observations, the simulated flux shows the similar spectrum profile from 10 keV to 100 keV, while the precipitated flux is smaller than the flux at the magnetosphere. The result indicates that LBC observed by the Van Allen Probes-A satellite is the main driver for the electron precipitations from 10 keV to 200 keV that are observed by EISCAT.

In order to investigate the reason for the different energy spectrum at sub-relativistic energy range between the magnetosphere and the ionosphere, we estimate the resonant

$$\omega - k_{\parallel} v_{\parallel} = \frac{|\Omega_e|}{\gamma}$$

energy of precipitating electrons. The first-order resonance condition addresses the electron scattering by whistler-mode waves propagating along the field line. Here, ω, $k_{\parallel}$, $v_{\parallel}$, Ω_e, and are the angular wave frequency, parallel wave number, parallel speed of the electron, and electron cyclotron angular frequency, respectively. Under the cold plasma approximation, the dispersion relation of the whistler-mode waves propagating parallel to the magnetic field line is

$$k_{\parallel} = \frac{\omega}{c}\sqrt{1 + \frac{\omega_{pe}^2}{\omega\left(|\Omega_e| - \omega\right)}}$$

where ω_{pe} is the electron plasma frequency. The loss-cone angle at the equator is evaluated as $\alpha_{loss} = \sin^{-1}\sqrt{B/B_a}$, where B_a is the field intensity at the atmospheric altitude. The parallel speed of electrons with the loss-cone pitch angle α_{lc} is

$$v_{\parallel,lc}^2 = \frac{p_e^2}{m^2\gamma^2}\left(1-\frac{B}{B_a}\right)$$

In the simulation of this study, it was assumed that LBC can propagate to the magnetic latitude less than 20 deg. **Figure 9** shows the resonant energy of electrons along the field lines due to whistler-mode waves as same plasma condition as the simulation. At higher latitudes, chorus waves can resonate with higher energy and cause pitch-angle scattering. The whistler-mode waves of $\omega = 0.2|\Omega_e|$ can resonate with 200 keV electrons at magnetic latitude of ~28 deg, whereas the waves of $\omega = 0.35|\Omega_e|$ can resonate with them at magnetic latitude of ~35 deg. Since the resonance condition for electrons above 100 keV is not satisfied when LBC propagates to the magnetic latitude less than 20 deg, the precipitated flux becomes significantly small at the energy above 100 keV. In fact, we confirmed that more energetic electrons precipitate into the ionosphere by the simulation, if LBC can propagate to high latitude larger than 20 deg.

As shown in Figure 1, we expect that the precipitations of sub-relativistic/relativistic electrons caused by LBC are always accompanied with the pulsating aurora and/or diffuse aurora, which occur along the same field line. And, the latitudinal distribution of LBC controls the maximum precipitating energy of electrons associated with the pulsating aurora.

Finally, we discuss the possible relationship between the microbursts of sub-relativistic/relativistic electrons and the pulsating aurora [see the recent review by Tsurutani et al., 2013]. There have been several reports on microbursts in the sub-relativistic [e.g., Parks, 1967, Lee et al., 2012] and relativistic energy range [e.g., Imhof et al., 1992, Nakamura et al., 1995]. The model of Miyoshi et al. [2010] has predicted the simultaneous precipitation of **wide energy electrons** associated with pulsating auroras, because the propagating whistler-mode chorus waves can resonate with electrons **for a wide energy range along the same field line**. **Although the measurements of this study did not identify the microbursts of sub-relativistic/relativistic electrons, we suggest that a common process of whistler-mode chorus wave–particle interactions causes the microbursts of sub-relativistic/relativistic electrons and the pulsating aurora, which are modulated by the repetition period of the chorus elements.**

It is worth noting that such energetic electron precipitation down to mesospheric altitudes is important with regard to the cause of significant ionization as well as the enhancement of NOx [e.g., Isono et al., 2014, **Anderson et al., 2014**]. We expect that sub-relativistic electron precipitation, being concomitant with pulsating auroras, would have significant impact on the variation of the upper-atmosphere composition. Data from future satellites such as the ERG satellite [Miyoshi et al., 2012] and sounding rocket observations for **a wide energy range** from a few keV to MeV will provide a unified picture for pulsating auroras and precipitations of relativistic electrons.

5. Conclusion

We examined the height-resolved electron density profile obtained using the EISCAT Tromsø VHF radar, which was associated with the pulsating aurora observed on **17 November 2012**. Electron density enhancements were clearly identified at altitudes >68 km in association with the pulsating aurora, suggesting the precipitation of electrons with **a wide energy range** of up to 200 keV. **The observations from the network of subionospheric radio wave receiver showed >50 keV electron precipitations from 01 MLT to 07 MLT, and the riometer observations confirmed the energetic electron precipitations during the period.** The Van Allen Probe-A satellite, which was very close to Tromsø during the time, observed rising tone emissions of the LBC waves. Comparing the energy spectrum at the magnetosphere observed by the Van Allen Probe-A and at the ionosphere estimated from the CARD inversion method with the EISCAT observation, the electron flux from a few keV to ~100 keV is almost same between them, indicating that the pitch angle scattering occurred in the strong diffusion up to ~100 keV. On the other hand, the electron flux above 100 keV at the ionosphere is smaller than that at the magnetosphere.

Using the Van Allen Probe-A satellite data, we conducted a computer simulation of the wave–particle interactions. The simulated electron energy spectrum at the ionosphereic altitude is well consistent with that estimated from the CARD inversion method, indicating that the observed LBC can cause the simultaneous precipitations of electrons at both tens of keV and a few hundred keV for the period with the pulsating aurora. The latitudinal distribution of LBC controls the resonant energy of electrons.

These results are evidence that pulsating auroras are caused by chorus wave–particle interactions. Furthermore, it was confirmed that whistler-mode chorus waves can cause the simultaneous precipitation of **wide energy electrons**. We suggest that the propagating whistler-mode chorus waves are a common process that simultaneously causes both the pulsating aurora and precipitation of sub-relativistic/relativistic electrons.

Acknowledgements.

Data of EISCAT radar used in this study were opened to the public via the EISCAT website (http://www.eiscat.se/raw/schedule/schedule.cgi). The quick look of all sky imager and the photometer data at Tromsø can be provided from the Solar-Terrestrial Environment Laboratory, Nagoya University, Japan (http://www.stelab.nagoya-u.ac.jp/~eiscat/prephoto_data.html). The Van Allen Probes data used in this study have been opened to the public from the university of Iowa, US (https://emfisis.physics.uiowa.edu/) and the Los Alamos National Laboratory, US (http://www.rbsp-ect.lanl.gov/). We are indebted to the director and staff of EISCAT for operating the facility and supplying the data. EISCAT is an International Association supported by China (CRIRP), Finland (SA), the Federal Republic of Germany (DFG), Japan (STEL and NIPR), Norway (NFR), Sweden (VR) and the United Kingdom (PPARC). We thank the institutes who maintain the IMAGE Magnetometer Array. A part of this work was carried out by the joint research program of the Solar-Terrestrial Environment Laboratory, Nagoya University. This study is supported by Grants-in-Aid for Scientific Research (23340146, 23224011, 24540478, 25302006, 08811147) of Japan Society for the Promotion of Science (JSPS). This work is also supported by JSPS Program for

Advancing Strategic International Networks to Accelerate the Circulation of Talented Researchers under grant number G2602 and research supported by the International Space Science Institute's (ISSI) International Team program.

References

Andersson et al.(2014), Missing driver in the Sun–Earth connection from energetic electron precipitation impacts mesospheric ozone, *Nature Communications*, doi:10.1038/ncomms6197.

Blake, J. B., et al. (2013), The magnetic electron ion spectrometer (MagEIS) instrumetns aboard the radiation belt storm probes (RBSP) spacecraft, *Space Sci. Rev.*, **179**, doi:10.1007/s11214-013-9991-8.

Brekke, A. et al.(1989), Auroral ionospheric conductance during disturbed condition, *Ann. Geophys.*, **7**, 269-280.

Clilverd, M. A., et al. (2009), Remote sensing space weather events: the AARDDVARK network, Space Weather, 7, S04001, doi: doi:10.1029/2008SW000412.

Cresswell-Moorcock, K., et al. (2013), A reexamination of latitudinal limits of substorm-produced energetic electron precipitation, *J. Geophys. Res. Space Physics*, 118, 6694-6705, doi:10.1002/jgra.50598.

Fujii, R., et al.(1995), Comparison between electron spectra calculated from EISCAT electron density profiles and those observed by the DMSP satellites, *J. Geomag. Geoelectr.*, **47**, 771-782.

Funsten, H. O. et al.(2013), Helium, Oxygen, Proton, and Electron (HOPE) Mass spectromenter for the radiation belt storm probes mission, *Space Sci. Rev.*, **179**, 423-484, doi:10.1007/s11214-013-9968-7.

Hikishima, M. et al. (2010), Microburst precipitation of energetic electrons associated with chorus wave generation, *Geophys. Res. Lett.*, **37**, L07103, doi:10.1029/2010GL042678.

Horne, R. B., and R. M. Thorne (2003), Relativistic electron acceleration and precipitation during resonant interactions with whistler-mode chorus, *Geophys. Res. Lett.*, **30**, 10, 1527, doi:10.1029/2003GL016973.

Imhof, W.L., et al.(1992), Relativistic electron microbursts, *J. Geophys. Res.*, **97**, 13829.

Isono, Y. et al.(2014), Variations of nitric oxide in the mesosphere and lower thermosphere over Antarctica associated with a magnetic storm in April 2012, *Geophys. Res. Lett.*, **41**, doi:10.1002/2014GL0598360.

Jones, S.L. et al.(2009), PFISR and ROPA observations of pulsating aurora, *J. Atm. Solar-Terr. Phys.*, **71**, 708-716.

Jones et al.(2009), PFISR and ROPA observations of pulsating aurora, *J. Atm. Solar-Terr. Phys.*, **71**, 708-716.

Kennel, C. F. (1969), Consequences of a magnetospheric plasma, *Rev. Geophys.*, 7(1, 2), 379–419, doi:10.1029/RG007i001p00379.

Kero, A., et al. (2014), Ionospheric electron density profiles inverted from a spectral riometer measurement, *Geophys. Res. Lett.*, 41, 5370-5375, doi:10.1002/2014GL060986.

Kletzing, C. A. et al.(2013), The electric and magnetic field instrument suite and integrated studies (EMFISIS) on RBSP, *Space Sci. Rev.*, 179, 127-181.

Lee, J.J., et al.(2012), Anisotropic pitch angle distribution of ~100 keV microburst electrons in the loss cone: Measurement from STSAT-1, *Ann. Geophys.*, **30**, 1567.

Lehtinen, M. S. and A. Huuskonen (1996), General incoherent scatter analysis and GUISDAP, *J. Atm. Terr. Phys.*, 58, 435-452.

Lessard, M.(2012), A review of pulsating aurora, in Auroral phenomenology and magnetospheric processes: Earth and other planets, edited by A. Keiling, E. Donovan, F. Bagenal, and T. Karlsson, AGU monograph series 197, doi:10.1029/2011GM001187.

Liang, J., et al.(2010), THEMIS observations of electron cyclotron harmonic emissions, ULF waves, and pulsating auroras, *J. Geophys. Res.*, **115**, A10235, doi:10.1029/2009JA015148.

Li, W., et al.(2010), THEMIS analysis of observed equatorial electron distributions responsible for the chorus excitation, *J. Geophys. Res.*, **115**, doi:10.1029/2009JA014845.

Li, W., et al.(2012), The origin of pulsating aurora: Modulated whistler mode chorus, in Auroral phenomenology and magnetospheric processes: Earth and other planets, edited by A. Keiling, E. Donovan, F. Bagenal, and T. Karlsson, AGU monograph series 197, doi:10.1029/2011GM001164.

Mauk, B.H. et al. (2012), Science objectives and radionale for the radiation belt storm probes mission, Space Sci. Rev., doi:10.1007/s11214-012-9908-y.

Meredith, N. P. et al. (2012), Global model of lower band and upper band chorus from multiple satellite observations, *J. Geophys. Res.*, **117**, A10225, doi:10.1029/2012JA017978.

Miyoshi, Y. et al.(2010), Time of flight analysis of pulsating aurora electrons, considering wave-particle interactions with propagating whistler mode chorus, *J. Geophys. Res.*, **115**, A10312, doi:10.1029/2009JA015127.

Miyoshi, Y. et al.(2012), The energization and radiation in geospace (ERG) project, in Dynamics of the Earth's radiation belts and inner magnetosphere, Geophys. Monograph Series, 199, edited by D. Summers, I. R. Mann, D. N. Baker, and M. Schulz, pp.103-116, AGU, Washington, D.C., doi:10.1029/2012BK001304.

Nakamura, R., et al.(1995), Relativistic electron precipitation enhancements near the outeredge of the radiation belt, Geophys. Res. Lett., 22, 1129-1132, doi:10.1029/95GL00378.

Nishimura, Y., et al.(2010), Identifying the driver of pulsating auroras, *Science*, **330**, 81.

Nishiyama, T., et al.(2011), The source region and its characteristic of pulsating aurora based on the Reimei observations, *J. Geophys. Res.*, **116**, A03226, doi:10.1029/2010JA015507.

Oyama, S. et al.(2014), Height-dependent ionospheric variations in the vicinity of nightside poleward expanding aurora after substorm onset, *J. Geophys. Res.*, doi:10.1002/2013JA019704.

Parks, G. K.(1967), Spatial characteristics of auroral-zone X-ray microburst, *J. Geophys. Res*., 72, 215.

Reinard, A. A., et al.(1997), Energy spectral characteristics of aurora electron microburst precipitation, *Geophys. Res. Lett.*, **24**, 611-614.

Rodger, C. J., et al. (2012), Contrasting the responses of three different ground-based instruments to energetic electron precipitation, *Radio Sci.*, 47, R2021, doi:10.1029/2011RS004971.

Saito, S., et al.(2010), A split in the outer radiation belt by magnetopause shadowing: Test particle simulations, *J. Geophys. Res.*, **115**, A08210, doi:10.1029/2009JA014738.

Saito, S., et al.(2012), Relativistic electron microbursts associated with whistler chorus rising tone elements: GEMSIS-RBW simulation, *J. Geophys. Res.*, **117**, A10206, doi:10.1029/2012JA018020.

Sandhl, I., et al.(1980), Rocket observations of precipitating electrons over a pulsating aurora, *Geophys. Res. Lett.*, **7**, 309-312, doi:10.1029/GL007i005p00309.

Santolik, O., et al. (2001), Complete wave-vector directions of electromagnetic emissions: Application to INTERBALL-2 measurements in the nightside auroral zone, *J. Geophys. Res.*, **106**, 13,191-13,201, 2001.

Santolik, O., et al. (2003), Singular value decomposition methods for wave propagation analysis, *Radio. Sci.*, **38**(1), 1010, doi:10.1029/2000RS002523.

Sato, N., et al.(2004), Generation region of pulsating aurora obtained simultaneously by the FAST satellite and a Syowa-Iceland conjugate pair of observations, *J. Geophys. Res.*, **109**, A10201, doi:10.1029/2004JA010419.

Semeter, J., and F. Kamalabadi (2005), Determination of primary electron spectra from incoherent scatter radar measurements of the auroral ***E*** region, *Radio Sci.*, **40**, RS2006, doi:10.1029/2004RS003042.

Simon Wedlund, M., et al. (2014), A statistical approach to determining energetic outer radiation belt electron precipitation fluxes, *J. Geophys. Res. Space Physics*, 119, 3961-3978, doi:10.1002/2013JA019715.

Spence, H. E. et al. (2013), Science goals and overview of the energetic particle, composition and thermal plasma (ECT) suite on NASA's radiation belt storm probes (RBSP) mission, Space Sci. Rev., doi:10.1007/s11214-013-0007-5.

Thorne, R.M., et al.(2010) , Scattering by chorus waves as the dominant cause of diffuse aurora precipitation, *Nature*, 467(7318), 943-946.

Tsurutani, B. T., et al.(2013), Energetic electron (>10 keV) microburst precipitation, ~5-15s X-ray pulsations, chorus, and wave-particle interactions: A review, *J. Geophys. Res.*, **118**, 2296-2312, doi:10.1002/jgra.50264.

Turunen, E., et al.(2009), Impact of different energies of precipitating particles on NOx generation in the middle and upper atmosphere during geomagnetic storms, *J. Atm. Solar-Terr. Phys.*, **71**, 1176-1189.

Figure Captions

Figure 1:

Schematic picture for the wave-particle interaction between the propagating chorus waves and **electrons**. (a) The chorus waves resonate with ~10 keV electrons at the equator. (b) The propagated chorus waves resonate with sub-relativistic/**relativistic** electrons at the higher latitudes.

Figure 2:

(a) Electron density profile observed by a vertical beam of the EISCAT Tromsø VHF radar on **16-17 November 2012**. Horizontal axis represents universal time; vertical axis denotes altitude. Color indicates the electron density. The figure is compiled from 1-min integrated data.

(b) Examples of all-sky images taken at Tromsø. Yellow and red rectangles indicate the direction of observation of the EISCAT VHF radar and photometer, respectively.

(c) Time variations of the photometer at 427.8 nm during the period.

Figure 3:

Electron density profile observed by EISCAT Tromsø VHF radar for period without (black) and with (red) the pulsating aurora. Horizontal axis represents electron density; vertical axis denotes altitude. (a) Density profiles from 60 to 200 km. (b) Same as (a) but from 60 to 80 km.

Figure 4:

Map of the AARDDVARK northern hemisphere network. Red and green points indicate the receiver and transmitter stations, respectively. Green lines correspond to the great circle paths between stations. The shaded region corresponds to the inferred precipitation region of >50 keV electrons during the event period.

Figure 5:

Trajectory of footprint of Van Allen Probe-A satellite for 04:00–05:00 UT on **17**

November 2012. The circle indicates the field-of-view of the all-sky imager at Tromsø.

Figure 6:

Plasma waves and energetic electron observations from the Van Allen Probe-A satellite for 04:00–08:00 UT on 17 November 2012. (a) Frequency-time diagram for electric fields obtained by EMFISIS. (b) Frequency-time diagram for magnetic fields. The white line is the local electron-gyro frequency. (c) and (d) Energy-time diagram at 90 deg and 24.5 deg obtained by ECT/MagEIS. (e) and (f) Energy-time diagram at 90 deg and 18.0 deg obtained by ECT/HOPE.

Figure 7:

Frequency spectrum and wave form for the magnetic field measurements obtained from EMFISIS wave burst mode **around** 04:50 UT on **17 November 2012**.

Figure 8:

(a) Frequency-time diagram of the LBC waves used in the GEMSIS-RBW simulation. **(b)** Energy spectrum at the magnetosphere observed by the Van Allen Probe-A satellite (blue triangle), at the ionosphere altitude estimated by the CARD inversion method using the EISCAT observation data (red triangle). Purple hexagons indicate the precipitated flux simulated by GEMSIS-RBW.

Figure 9:

Latitudinal profile of electron resonant energy, considering the first-cyclotron resonance condition with whistler-mode waves. Black and red lines represent resonance with whistler-mode waves of $\omega = 0.2\omega_{ce}$ and $\omega = 0.35\omega_{ce}$, respectively. Dashed line indicates the energy of 200 keV, i.e., the maximum precipitation energy of the pulsating aurora estimated from the EISCAT observations.

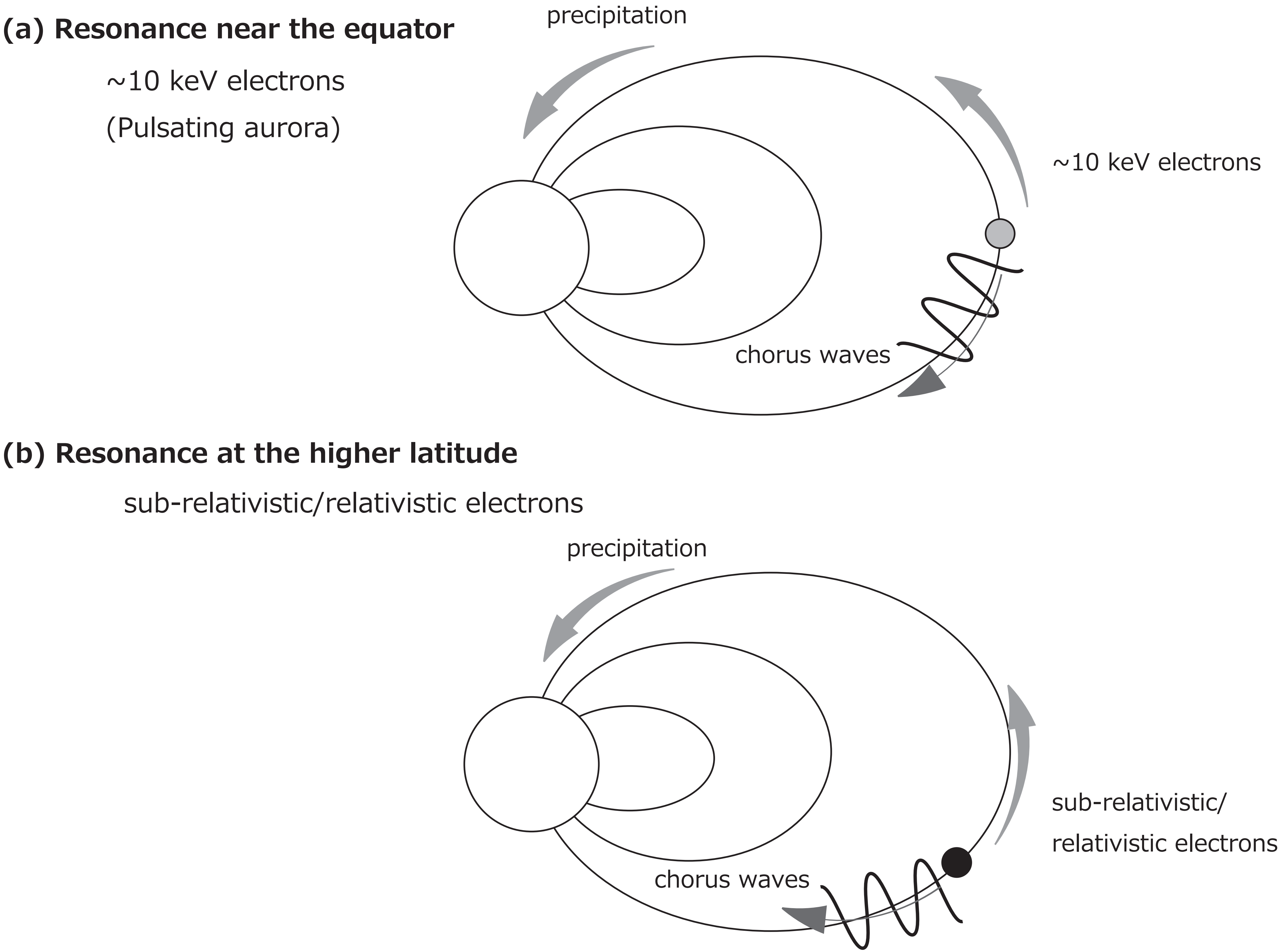
(a) Resonance near the equator
~10 keV electrons
(Pulsating aurora)
precipitation
~10 keV electrons
chorus waves
(b) Resonance at the higher latitude
sub-relativistic/relativistic electrons
precipitation
sub-relativistic/
relativistic electrons
chorus waves

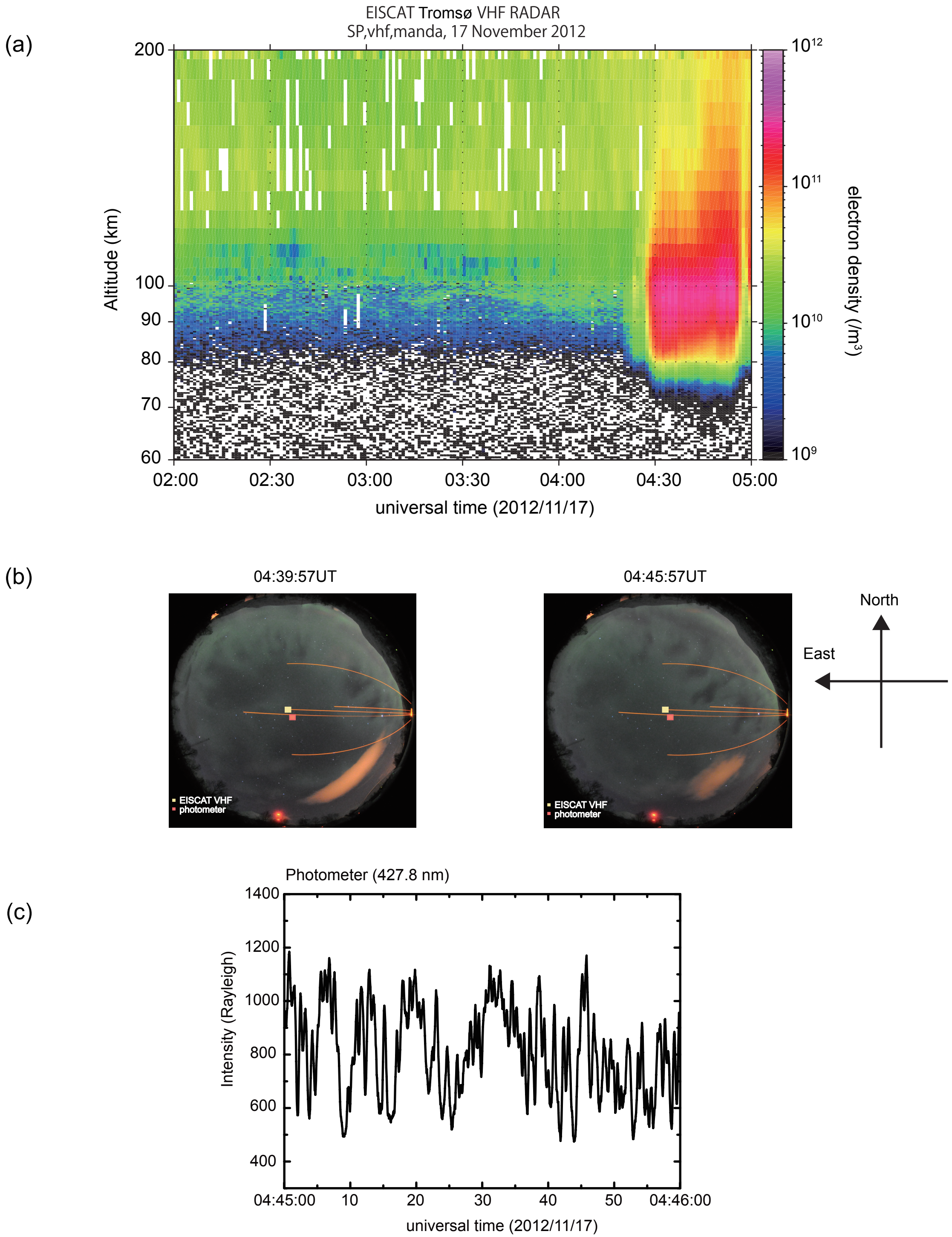

(a)
EISCAT Tromsø VHF RADAR
SP,vhf,manda, 17 November 2012
Altitude (km)
200
100
90
80
70
60
02:00
02:30
03:00
03:30
04:00
04:30
05:00
universal time (2012/11/17)
10^{12}
10^{11}
10^{10}
10^{9}
electron density (/m^3)
(b)
04:39:57UT
04:45:57UT
EISCAT VHF
photometer
North
East
(c)
Photometer (427.8 nm)
Intensity (Rayleigh)
1400
1200
1000
800
600
400
04:45:00
10
20
30
40
50
04:46:00
universal time (2012/11/17)

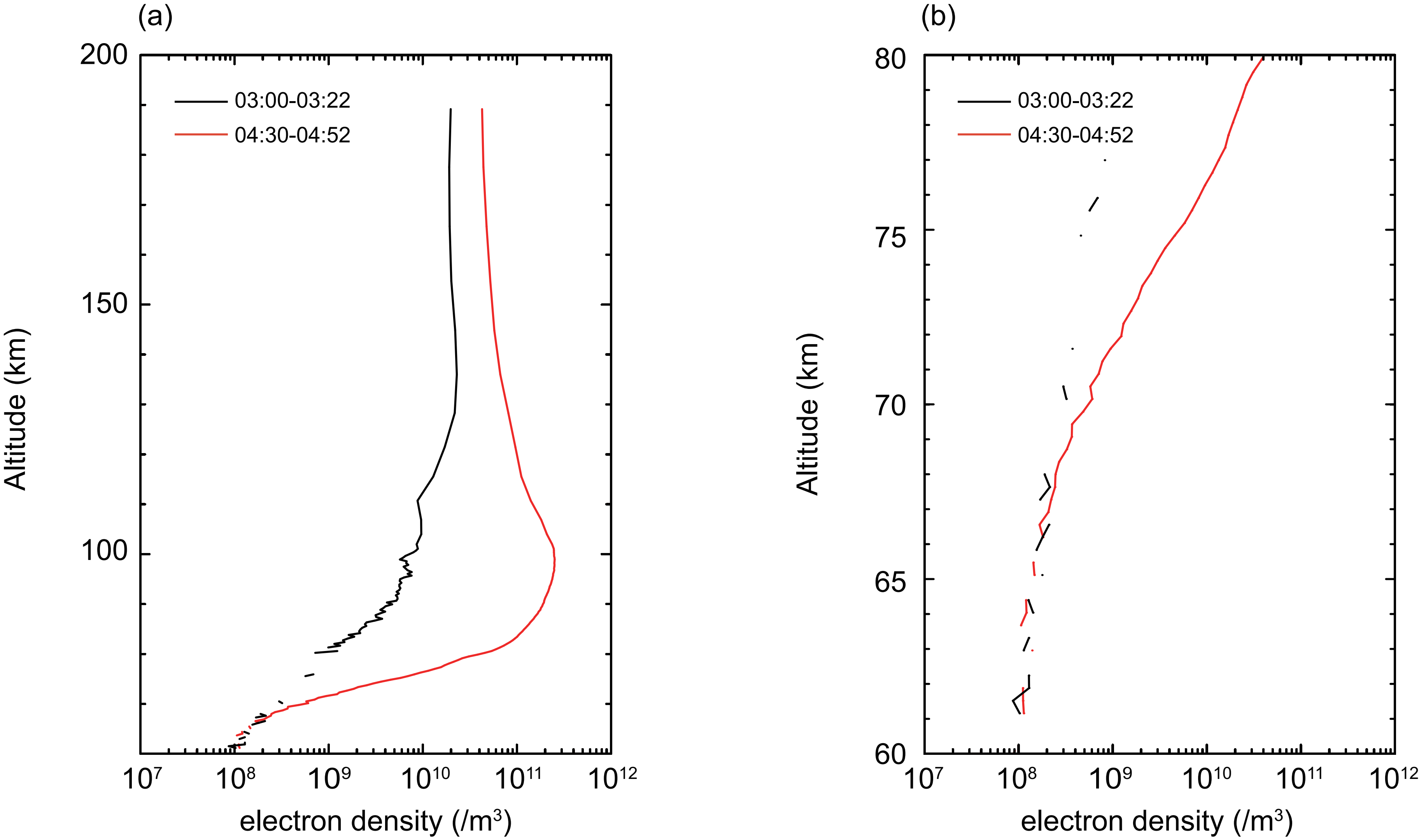

(a)
(b)
03:00-03:22
04:30-04:52
03:00-03:22
04:30-04:52
Altitude (km)
Altitude (km)
200
150
100
80
75
70
65
60
10^7
10^8
10^9
10^{10}
10^{11}
10^{12}
electron density ($/m^3$)
electron density ($/m^3$)

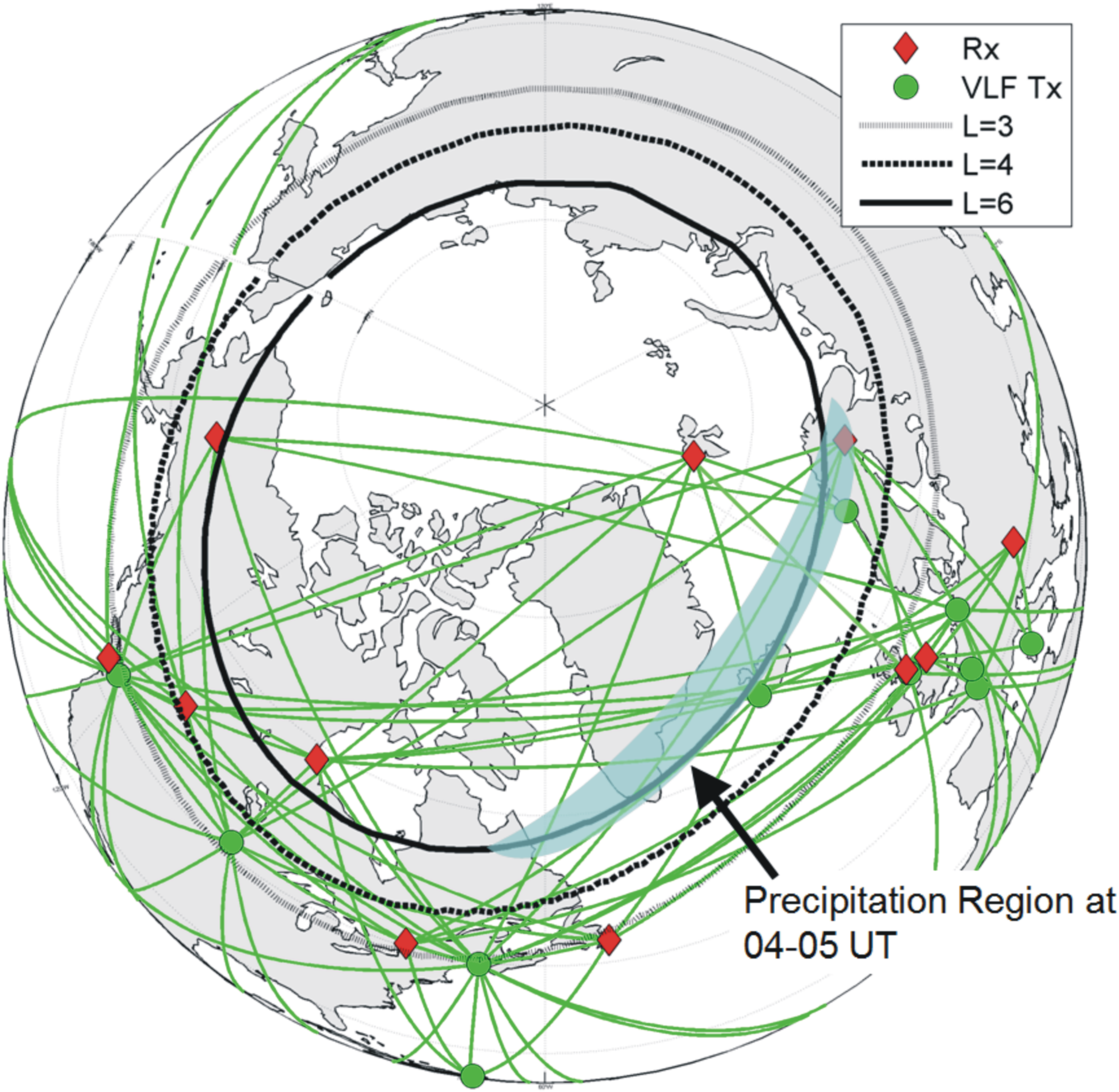

Rx
VLF Tx
L=3
L=4
L=6
Precipitation Region at
04-05 UT

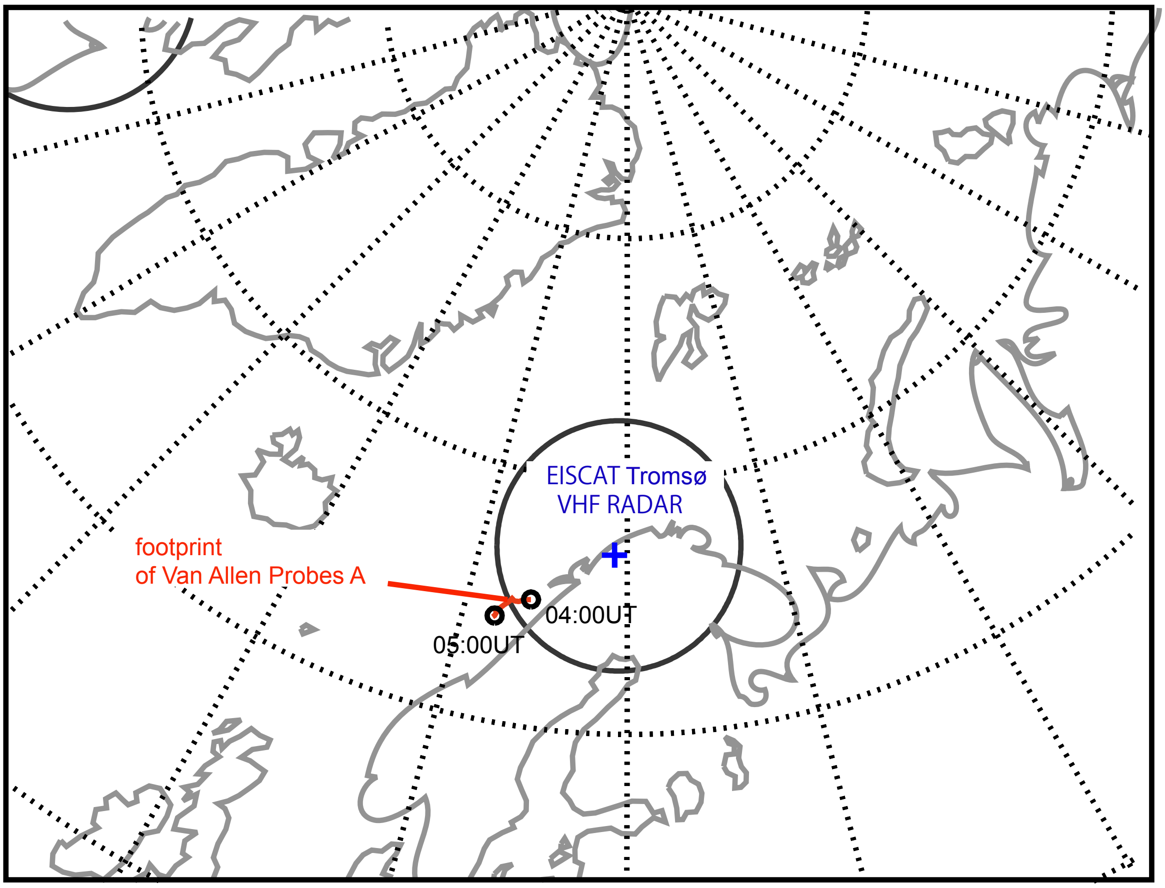
EISCAT Tromsø
VHF RADAR
footprint
of Van Allen Probes A
04:00UT
05:00UT

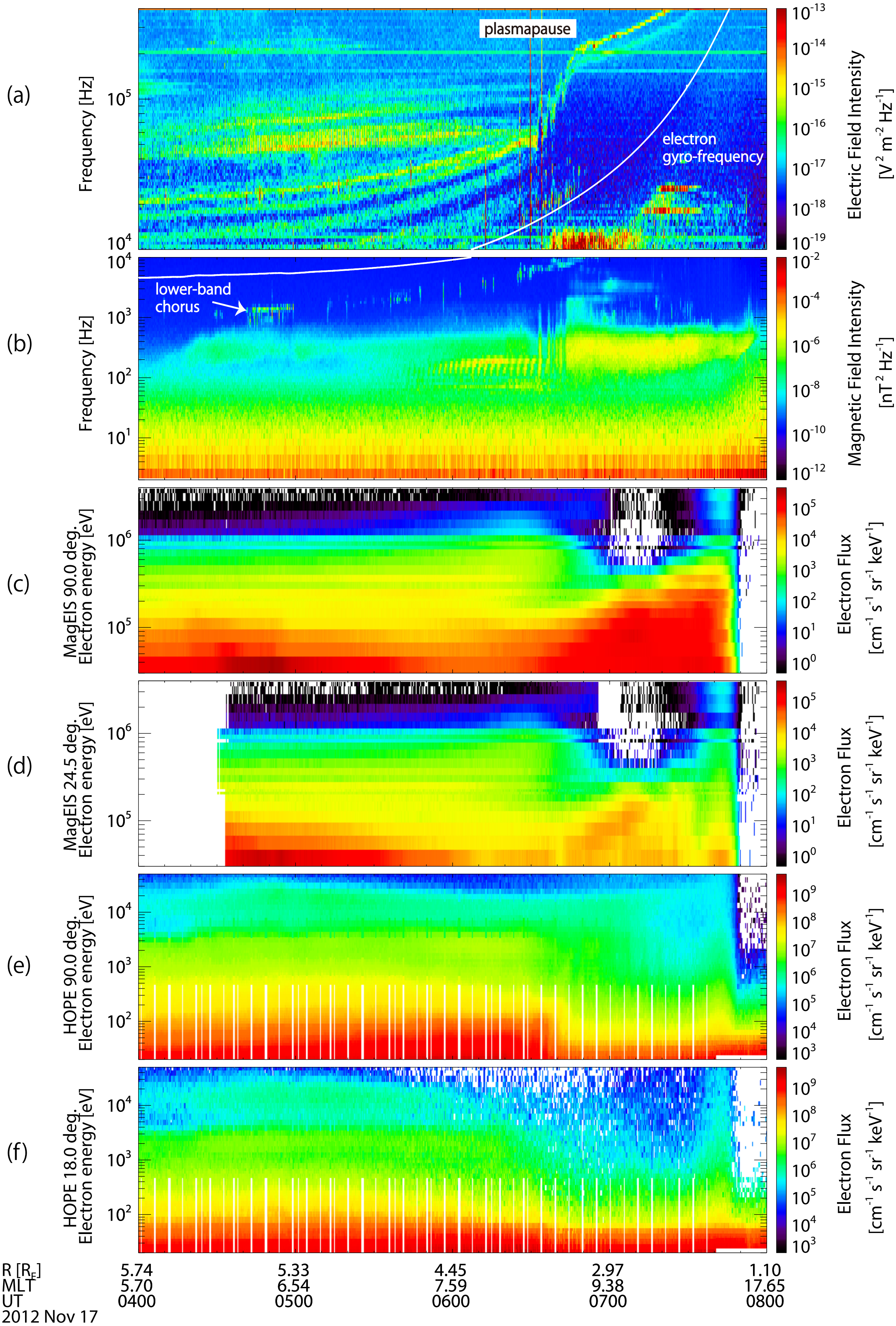

(a)
(b)
(c)
(d)
(e)
(f)
plasmapause
electron gyro-frequency
lower-band chorus
Frequency [Hz]
Electric Field Intensity [V^2 m^-2 Hz^-1]
Magnetic Field Intensity [nT^2 Hz^-1]
MagEIS 90.0 deg. Electron energy [eV]
MagEIS 24.5 deg. Electron energy [eV]
HOPE 90.0 deg. Electron energy [eV]
HOPE 18.0 deg. Electron energy [eV]
Electron Flux [cm^-1 s^-1 sr^-1 keV^-1]
R [R_E] 5.74 5.33 4.45 2.97 1.10
MLT 5.70 6.54 7.59 9.38 17.65
UT 0400 0500 0600 0700 0800
2012 Nov 17

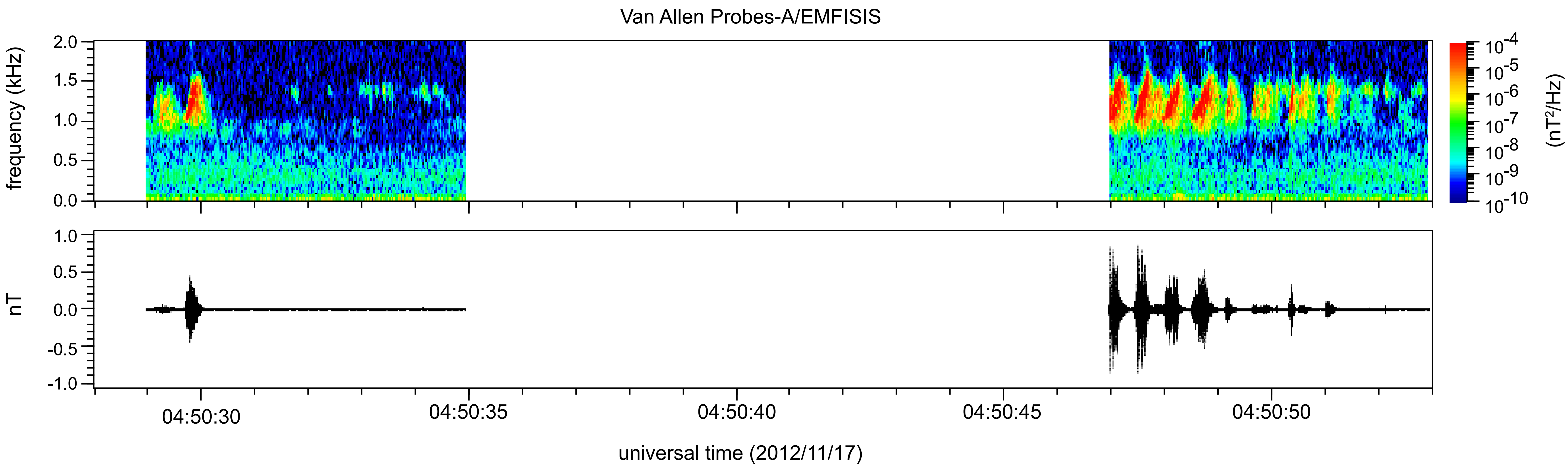

Van Allen Probes-A/EMFISIS
frequency (kHz)
2.0
1.5
1.0
0.5
0.0
10^{-4}
10^{-5}
10^{-6}
10^{-7}
10^{-8}
10^{-9}
10^{-10}
(nT^2/Hz)
nT
1.0
0.5
0.0
-0.5
-1.0
04:50:30
04:50:35
04:50:40
04:50:45
04:50:50
universal time (2012/11/17)

(a)

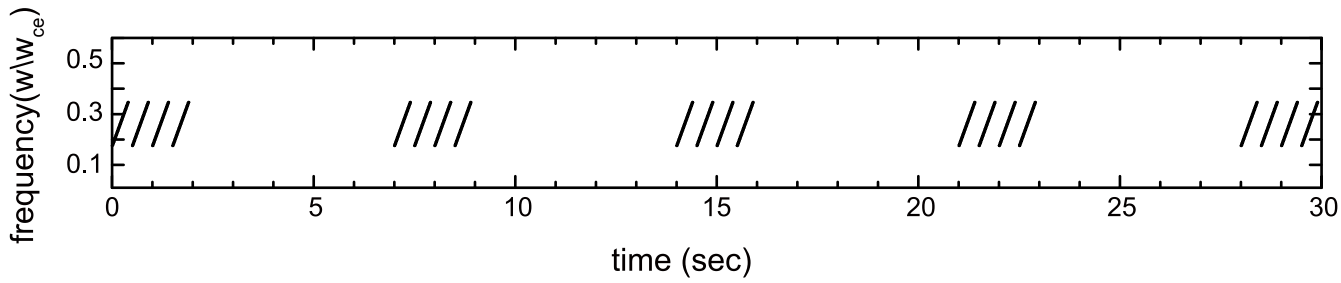
frequency(w\w_ce)
0.5
0.3
0.1
0
5
10
15
20
25
30
time (sec)

(b)

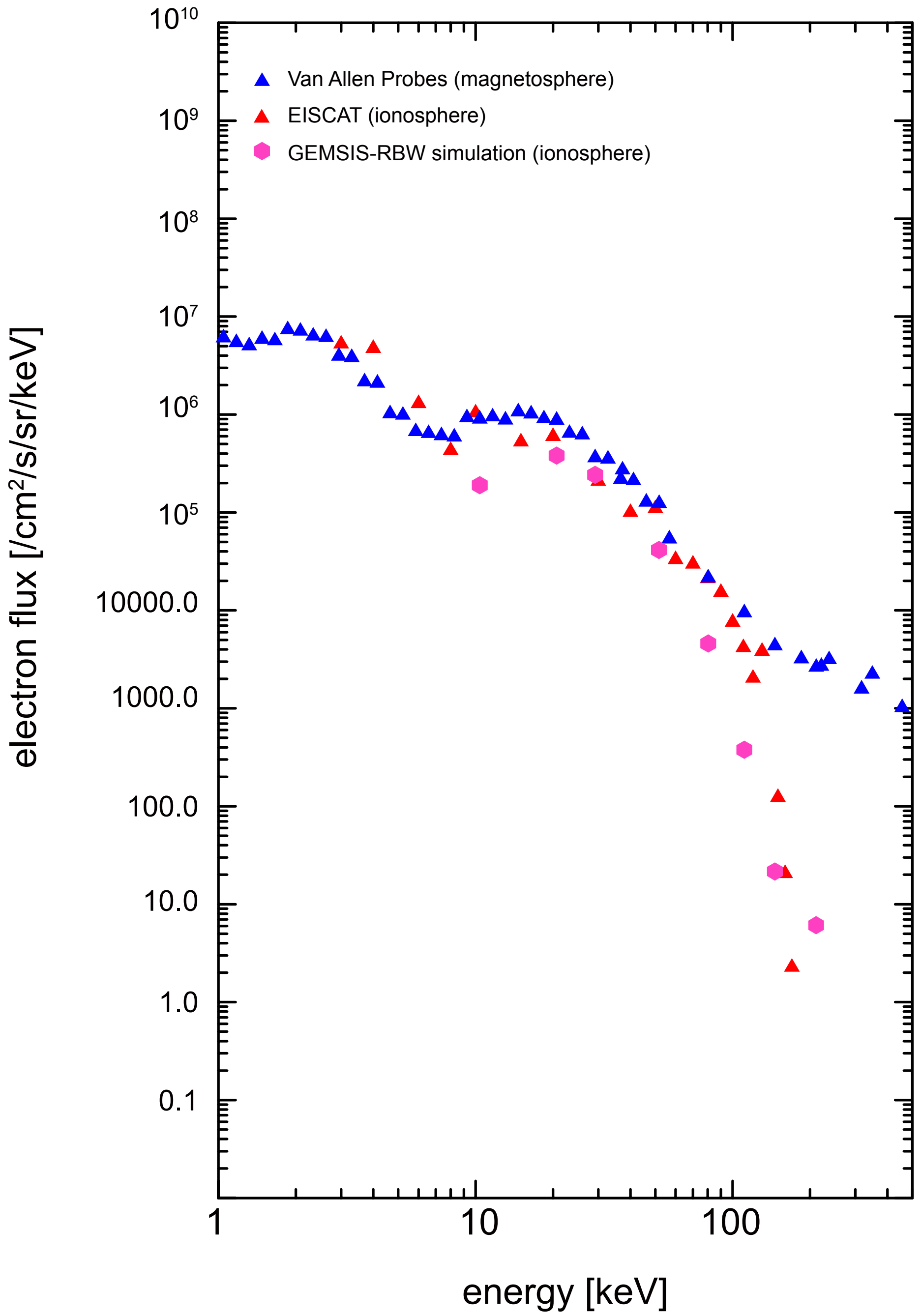
10^10
10^9
10^8
10^7
10^6
10^5
10000.0
1000.0
100.0
10.0
1.0
0.1
Van Allen Probes (magnetosphere)
EISCAT (ionosphere)
GEMSIS-RBW simulation (ionosphere)
electron flux [/cm²/s/s/sr/keV]
1
10
100
energy [keV]

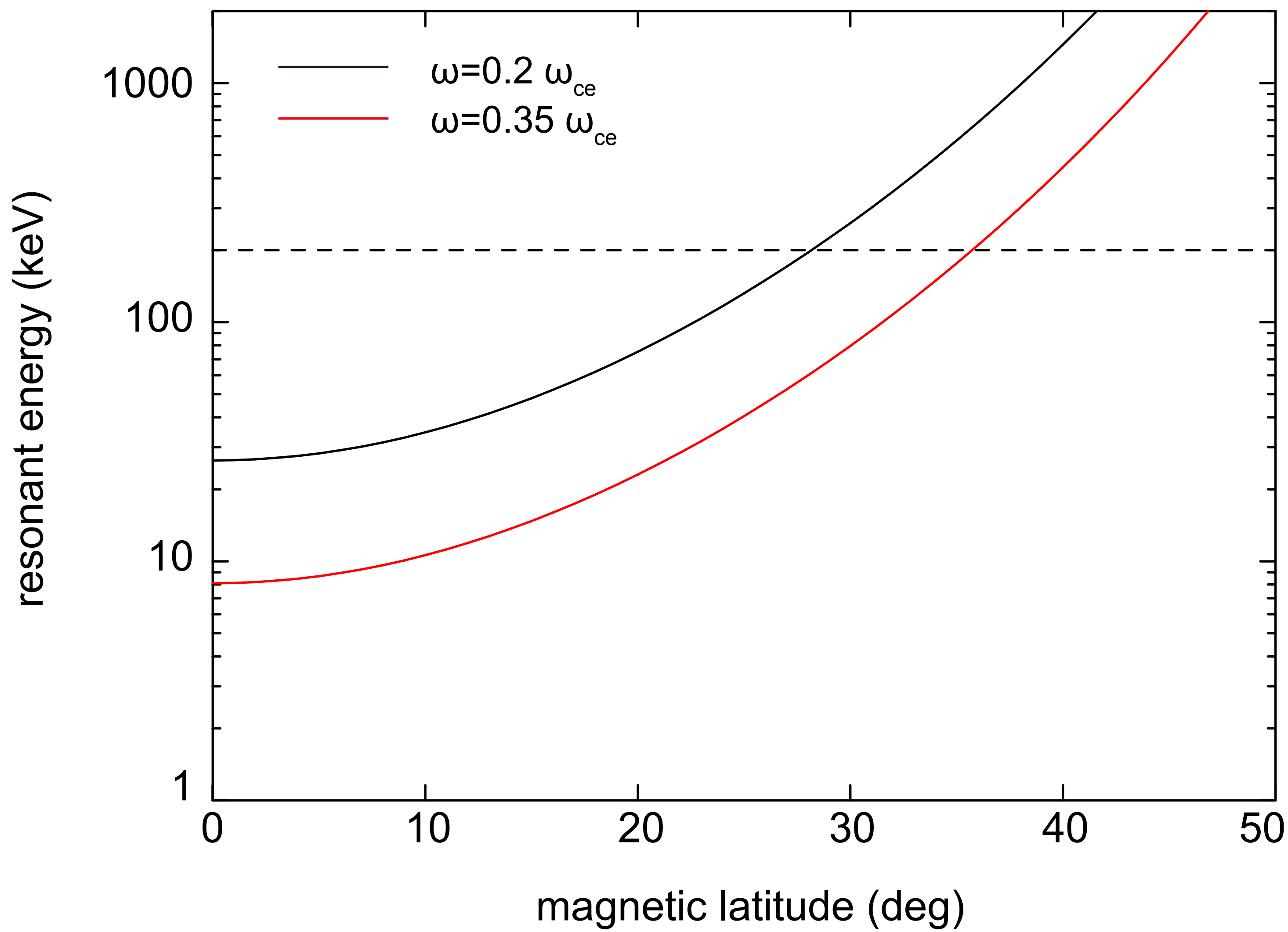
ω=0.2 ω_ce
ω=0.35 ω_ce
1000
100
10
1
resonant energy (keV)
0
10
20
30
40
50
magnetic latitude (deg)